An integrated Artificial Intelligence Framework for COVID-19 Classification and Detection Using Chest X-ray Radiographs

Xin Tie[1], Xin Yuan[2], Yuan Chen[3]

1. Department of Medical Physics, xtie@wisc.edu
2. Department of Computer Science, xyuan46@wisc.edu
3. Department of Computer Science, chen2243@wisc.edu

Abstract

Since the outbreak of COVID-19 pandemic in 2019, it has put the healthcare system under enormous pressure. As a routine screening tool, chest x-ray (CXR) imaging is now used in patient management along with thoracic CT. It also has potential use in patient triage due to fast acquisitions and wide availability. In this work, we present an integrated artificial intelligence (AI) framework for the classification and detection of COVID-19 using CXR images, enabling efficient patient triage and more confident diagnosis. The proposed framework is evaluated in multiple datasets, demonstrating the potential to provide clinical benefits and improve patient outcomes.

1. Introduction

At the end of 2019, a novel coronavirus emerged and quickly spread around the world as a pandemic. In February 2020, the World Health Organization (WHO) designated the disease COVID-19, standing for coronavirus disease 2019 [1]. Currently, the gold standard for identifying COVID-19 is the reverse transcription polymerase chain reaction (RT-PCR) test [2]. In addition to PCR test, diagnostic imaging, such as chest radiography (CXR), were widely used in the early pandemic, providing additional ways of COVID-19 diagnosis. But now, due to low sensitivity, it mainly serves as a tool for monitoring patients with severe or worsening respiratory symptoms [3]. Another potential application is to triage first-admitted patients with suspected COVID-19 [4] since chest x-ray imaging has unique advantages: (1) it is a super-fast non-invasive modality and (2) almost all clinics and hospitals are equipped with stationary and mobile radiography units. However, radiographic signs of COVID-19, such as bandlike ground-glass opacity or consolidation, are non-specific and can be observed in other viral illnesses as well [5], posing a challenge for radiologists to interpret. AI methods, especially deep learning, have shown considerable promise in medical applications. They can be quickly adapted to tirelessly learn the correlations between radiographic features and pathological labels (i.e., RT-PCR results), thereby optimizing the clinical workflow by prioritizing severely infected patients. When radiologists interpret chest radiographs, there exists nonnegligible intra- and inter-variability [6]. To handle this and improve the efficiency of diagnostic services, computer-aided detection (CAD) tools emerged to help radiologists diagnose patients more confidently along with other medical information. These tools usually localize some regions with suspected abnormalities, drawing radiologists' further attention.

Starting from the early pandemic, researchers have rushed to develop AI-based tools for COVID-19 diagnosis and prognosis. Many of them [7-12] focused on identifying COVID-19 pneumonia from Non-COVID-19 pneumonia or other acute pulmonary diseases, such as tuberculosis, pneumothorax, etc. Some studies [13] tried to provide severity scores based on the opacity level in various lung lobes. Other works [14] incorporated information from multiple modalities to predict potential needs, such as oxygen, for patients who were admitted to emergency departments. It allowed limited resources during the pandemic to be distributed more efficiently.

In this work, we designed an integrated AI framework for COVID-19 classification and detection using chest x-ray images for patient triage. It allowed COVID-19 positive patients to be treated as early as possible. Additionally, a COVID-19 pneumonia detection network was developed to predict suspected locations of abnormalities with bounding boxes, helping clinicians better deliver the treatment based on patients' severity.

2. Dataset

2.1 Data for COVID-19 classification

To develop the classification model, a large-scale CXR dataset was collected from the Henry Ford (HF) healthcare system [15]. All included patients were diagnosed with COVID-19 or Non-COVID-19 based on the RT-PCR test. To avoid potential source bias, both COVID-19 positive and negative data were acquired within the same time frame, i.e., from March 2020 to October 2020. To benchmark the performance of the classification model, all data from October were held out for internal testing, while others were used for training and validation. Concretely, the training and validation datasets consisted of 6,689 COVID-19 positive CXRs from 3,264 patients and 10,848 COVID-19 negative CXRs from 4,802 patients. The hold-out test set (denoted as HF hold-out dataset) contained 466 COVID-19 positive CXRs from 334 patients and 5,224 COVID-19 negative CXRs from 3,120 patients.

Generalizability testing is always an essential component of demonstrating clinical utility. In this work, we used a public COVID-19 CXR dataset from Valencian Region,

The source code is available at https://github.com/xtie97/COVID-19-classification-and-detection

Spain [16]. All data were collected between February and April 2020. RT-PCR test results were generously provided by authors and served as labels in our work. This external testing set (denoted as BIMCV dataset) consisted of 3,144 COVID-19 positive CXRs from 2,004 patients and 3,335 COVID-19 negative CXRs from 2,365 patients.

2.2 Data for COVID-19 pneumonia detection

To train and evaluate the detection network, we used a public COVID-19 CXR dataset [17] with well-annotated bounding boxes provided by a group of radiologists. The suspected locations of COVID-19 pneumonia were enclosed by these bounding boxes. This dataset was released by the Radiological Society of North America (RSNA) in 2021 as a grand challenge. The whole dataset consisted of 6334 independent CXR images. To evaluate the performance, 10% of the data (633 images) were randomly sampled and never touched during the training stage. The remaining data were divided into training (5131 images) and validation sets (570 images) for model development.

3. Methods

3.1 Proposed integrated AI framework

After patients are admitted to the hospital, clinicians may send them to the radiography unit for a quick screening based on their symptoms. Then patients have to wait for radiology reports from thoracic radiologists. This typical first-in-first-out flow is inefficient because it may miss the best time to treat severe patients infected with COVID-19. Therefore, a classification model is introduced for better patient triage. The acquired chest x-ray images are fed into the model, which predicts whether these patients are positive or negative. Based on the predictions, the radiologists' worklist is updated, and suspected positive patients are prioritized. Meanwhile, these chest x-ray images are processed by a COVID-19 pneumonia detection network. It draws some bounding boxes related to potential abnormalities with confidence scores before transferring images to radiologists. This process enables radiologists to make diagnoses more confidently and quickly. As a result of better triage and diagnosis, more patients can receive the best care before the severe effects of the virus take place.

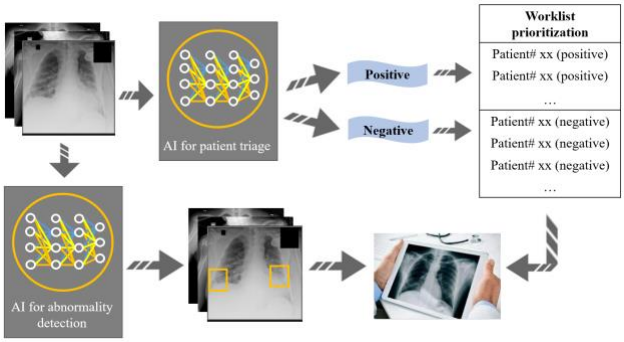

Figure 1: the proposed AI framework to optimize the clinical workflow and help radiologists diagnose patients more confidently and quickly

3.2 COVID-19 classification models

Before CXR images were fed into the network, a few pre-processing steps were required to convert clinical DICOM files to desired model input. Concretely, DICOM images were resized to 1024×1024 using bilinear interpolation and converted to 8-bit grayscale images. Then they were processed by a segmentation network to get lung masks. Based on the generated masks, images were cropped to only include lungs, while the background anatomies, such as shoulders and abdomens, were excluded. After the cropping, all images were resized to 224×224, the same as the typical image size in ImageNet.

Multiple model architectures were explored to train the classification network, including VGG-16 [18], SqueezeNet [19], DenseNet-121 [20], EfficientNet [21], and Swin Transformer-B [22]. All these architectures were widely applied to various classification tasks in the medical domain. To boost the performance, progressive learning was used by carrying through 3 steps: pretraining models on ImageNet [23] and the NIH chest x-ray dataset [24] and then finetuning on the COVID-19 dataset. Adam optimizer [25] with an initial learning rate of 5×10^{-5} was used to minimize the binary cross-entropy (BCE) loss. If the validation loss did not decrease for 3 epochs, the learning rate was reduced to one-half of the current value. Multiple image augmentation techniques were applied, including random horizontal flipping and rotation, to regularize the model training. Final predictions were obtained by the model ensembles, which involved 5 models trained with identical hyperparameters. The area under the receiver characteristic curve (AUC) was used as the metric to evaluate the model performance.

3.3 COVID-19 pneumonia detection models

Similar to the pre-processing in the classification part, all images were first converted from DICOM to 1024×1024 png files and then cropped to only include lungs and bounding boxes. The cropped images were resized to 512×512 as model input.

The COVID-19 pneumonia detection network was based on a one-stage object detection technique, YOLOv5 [26]. It was first released in 2020 and soon became popular due to its speed and accuracy. Three different model sizes, i.e., YOLOv5-small, YOLOv5-medium, and YOLOv5-large, were investigated to help us figure out the best model capacity. To fully take advantage of progressive learning, we pretrained the detection network on the COCO dataset [27] and the 2018 Kaggle pneumonia detection dataset [28], then finetuned on the RSNA COVID-19 pneumonia detection dataset [17]. The Adam optimizer [25] with initial learning of 1e-3 was used across all three model sizes. The loss function was defined as a combination of mean squared loss for bounding box regression (weight: 0.05) and binary cross entropy loss for the confidence of object presence (weight:1.0). To evaluate the detection models, mean average precision (mAP) at different IoU thresholds was used. The threshold values ranged from 0.4 to 0.7 with a step

size of 0.05.

3.4 Simulation of radiology turn-around time (RTAT)

To demonstrate the potential benefits of deploying our model in the clinical system, a simulation study was performed on the HF hold-out dataset to compute report turn-around time (RTAT) for COVID-19 findings in the CXRs. The RTAT simulation was characterized by the time of acquisition and time of report [29, 30]. The first one can be obtained from the metadata, while the second one should be determined by the prioritized worklist and the required time for finalizing a CXR report.

As shown in Figure 1, after being processed by the classification model, acquired CXR images were inserted into the COVID-19 dynamic queue or the Non-COVID-19 queue, depending on the predictions. Two dynamic queues were combined to form a single worklist with COVID-19 patients having higher priorities. It was updated every minute, and after that, the system assigned the first few CXRs to available radiologists.

For simplicity, a Gaussian distribution with an average reporting time of 15 min and a standard deviation of 2 min was used to model the time deltas between 2 CXR reports. Two virtual radiologists were assumed to perform diagnosis day and night (24h per day without rest). To reduce the RTAT of false negative cases, a maximum waiting time of 300 min was applied. For comparison, we simulated the standard first-in, first-out (FIFO) scenario to approximate the historical clinical workflow.

4. Results

4.1 Performance of COVID-19 classification

As shown in Table 1, Swin-transformer achieved the highest AUC among all architectures on both internal and external datasets. However, other CNN-based models were not significantly inferior to this transformer-based model except SqueezeNet. Potential reasons include pretraining in the large-scale NIH CXR dataset, indeterminate correlations between pathological labels, and radiographic features. The gap between the HF hold-out and the BIMCV dataset was small, indicating that our models achieved generalizability despite different populations and imaging system vendor distributions in these two testing datasets.

	VGG-16	SqueezeNet	DenseNet-121	EfficientNet	Swin Transformer-B
Number of parameters	138 M	1 M	8 M	54 M	88 M
HF hold-out dataset	0.818 [0.803, 0.833]	0.781 [0.766, 0.795]	0.819 [0.805 0.834]	0.822 [0.807, 0.837]	0.826 [0.811, 0.841]
BIMCV dataset (external test)	0.809 [0.800, 0.819]	0.772 [0.762, 0.783]	0.811 [0.802 0.820]	0.805 [0.795, 0.814]	0.815 [0.806, 0.824]

Table 1: internal and external testing performance among different model architectures

Figure 2 presents how AUC changes with training data sizes in both internal and external datasets. DenseNet-121 was used as a baseline model for this study. The total number of patient data involved in training ranged from 100 to 6000. Based on these two plots, we observed that a significant performance gain occurred when the training data sizes increased from 100 to 800 patients. Adding more data only marginally improved the performance. Another experiment was done to test how important proper pretraining was. If the models were only pre-trained on ImageNet, even using all training data still cannot beat the models pretrained on the NIH dataset and finetuned on one-sixth of training data (roughly 1000 patients).

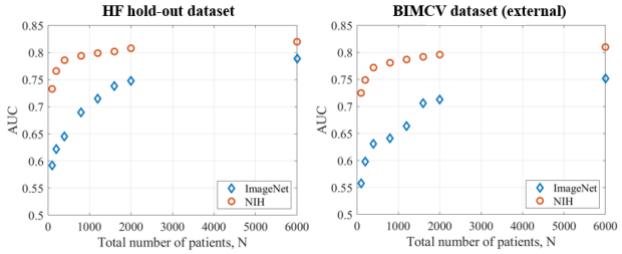

Figure 2: AUC changes with training data size.

4.2 Performance of COVID-19 pneumonia detection

Table 2 lists the detection performance among three different model sizes. YOLOv5-medium achieved slightly higher mAP than others. With pretraining on the 2018 Kaggle pneumonia dataset, the mAP was further improved.

		mAP (0.4-0.7)	
Model size	Number of parameters	Without pre-training	With pre-training
Yolov5-Small	7 M	0.478	0.487
Yolov5-Medium	21 M	0.496	0.501
Yolov5-Large	46 M	0.482	0.495

Table 2: COVID-19 pneumonia detection performance among different model sizes with and without pretraining

In Figure 3, two representative true positive cases are shown in the 1st row. The network captured all suspected locations of COVID-19 pneumonia. The 2nd row presents one false negative (FN) case on the left and one false positive (FP) case on the right. In the FN case, the network missed the abnormality located at the boundary of the left lung and the heart. It was subtle and not a typical region for COVID-19 pneumonia, given that the common radiographic sign was peripheral ground-glass opacity. In the FP case, the network gave a high confidence score to the opacity located at the lower right lobe, but this region was somehow not labelled by radiologists.

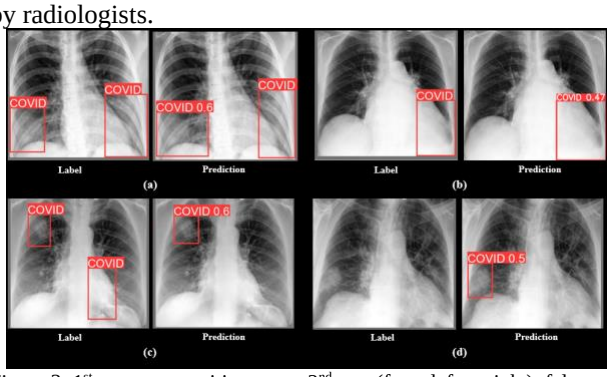

Figure 3: 1st row: true positive cases. 2nd row (from left to right): false negative and false positive cases. The threshold for confidence scores was set as 0.25 and the IoU threshold for non-max suppression was 0.1.

The source code is available at https://github.com/xtie97/COVID-19-classification-and-detection

4.3 Correlation between the COVID-19 classification and detection

In this section, we investigated how the classification performance was correlated with the detection results. The whole BIMCV dataset was divided into 3 subsets based on the number of bounding boxes drawn in CXR images by the detection model, as shown in Table 3. As the number of boxes increased, AUC increased as well, indicating that more abnormalities present in images may help the classification model identify COVID-19 from Non-COVID-19. When no abnormalities can be detected by the network, it would be difficult for the classification model to make a correct judgment (AUC=0.690).

# of bounding boxes	Ratio	AUC
= 0	24%	0.690
= 1	34%	0.790
≥ 2	42%	0.822
All	100%	0.811

Table 3: Classification performance changes with the number of bounding boxes. "Ratio" means the percentage of data in each subset with respect to the whole testing cohort.

4.4 Potential clinical benefits quantified by RTAT

RTAT simulation reflected the efficiency of the given clinical workflow. Table 4 shows the reduction of RTAT in COVID-19 positive patients if the classification model was deployed in a virtual clinical environment. The operating point for the model was chosen to be 0.7, the sensitivity was 0.51, and the specificity was 0.94. The RTAT of 50% positive patients decreased to one-half of the required time under the first-in-first-out (FIFO) scenario. At least 75% of positive patients could receive their care earlier with AI-aided triage. The waiting time of COVID-19 negative patients was not extended significantly (p-value=0.33) due to the high specificity of the model. All these results demonstrated that our framework reduced the RTAT markedly for COVID-19 positive patients with a mild impact on negative patients.

	COVID-19 (min)		
	Median	75 percentile	95 percentile
AI-aided triage	68	285	483
FIFO	149	333	474
Improvements	2.19	1.17	0.98
p-value		0.0004	
	Non-COVID-19 (min)		
	Median	75 percentile	95 percentile
AI-aided triage	148	330	477
FIFO	146	318	473
Improvements	0.99	0.96	0.99
p-value		0.33	

Table 4: Potential RTAT reduction among COVID-19 positive patients if the classification model was applied.

5. Discussion

In this work, the classification model was developed for patient triage, achieving an AUC of 0.826 in the HF hold-out dataset and 0.815 in the BIMCV dataset using the Swin Transformer. Even though this transformer-based model had many impressive results in various real-world datasets and in multiple vision tasks, it could not beat other CNN-based models with a significant improvement. The reasons may lie in an unclear correlation between PCR tests and radiographic features, pretraining in a large-scale and relevant dataset, the low resolution of input images (i.e., 224×224), etc.

In modern deep learning, people expect a good performance brought by a large and diverse dataset. Based on our experiments, with proper pretraining, a small portion of high-quality training data can offer a baseline performance and enable generalizability as well.

For the COVID-19 pneumonia detection task, YOLOv5-Medium with pretraining achieved slightly better mAP than other settings. If the task was not only to identify suspected locations but also classify the abnormalities into several categories, the one-stage detection technique studied in this work may not achieve competitive performance compared with two-stage object detection techniques, such as faster RCNN [31] and mask RCNN [32]. So far, subtle findings and irregular locations of abnormalities in CXR images were still challenging for our detection model. In the future, we would like to explore more advanced techniques and investigate some attention mechanisms that can guide the model to learn subtle features.

The last step in our work was to demonstrate the clinical utility of the proposed AI framework. To accomplish this, radiology report turn-around time was simulated for the HF-hold out dataset, which contained all data from October 2020. With AI-aided triage, about 75% of COVID-19 positive patients can receive further treatment and care earlier compared to FIFO, indicating that our framework can be more efficient than the typical clinical workflow. In the future, more factors will be incorporated into our simulation because clinical environments are way more complicated.

In addition to the limitations mentioned above, COVID-19 variants and level of immunity due to vaccination or prior infection were not considered in this work. Further investigation into the evolution of COVID-19 pneumonia and how it impacts AI models is needed.

6. Conclusion

In conclusion, an integrated AI framework was developed for COVID-19 classification and detection using CXR images. It can be used to optimize the clinical workflow by prioritizing positive and severe patients. It also captured suspected locations of abnormalities, helping radiologists diagnose patients more quickly and confidently.

The source code is available at https://github.com/xtie97/COVID-19-classification-and-detection

Author contributions: Problem formulation, X.T.; study design, all authors; literature research, all authors; experimental studies, all authors; statistical analysis, all authors; manuscript drafting and editing, all authors.

References

[1] World Health Organization, "WHO COVID-19 Dashboard," [Online]. Available: https://COVID19.who.int/. [Accessed 8 2021].

[2] U.S. Food and Drug Administration, "Accelerated emergency use authorization (EUA) summary COVID-19 RT-PCR test (Laboratory Corporation of America)," U.S. Food and Drug Administration, Silver Spring, MD, 2021.

[3] Y.-F. Tu, C.-S. Chien, A. A. Yarmishyn, Y.-Y. Lin, Y.-H. Luo, Y.-T. Lin, W.-Y. Lai, D.-M. Yang, S.-J. Chou, Y.-P. Yang, M.-L. Wang and S.-H. Chiou, "A Review of SARS-CoV-2 and the Ongoing Clinical Trials," International journal of molecular sciences, vol. 21, no. 7, p. 2657, 2020.

[4] Y. Oh, S. Park and J. C. Ye, "Deep Learning COVID-19 Features on CXR Using Limited Training Data Sets," in *IEEE Transactions on Medical Imaging*, vol. 39, no. 8, pp. 2688-2700, Aug. 2020, doi: 10.1109/TMI.2020.2993291.

[5] J. P. Kanne, H. Bai, A. Bernheim, M. Chung, L. B. Haramati, D. F. Kallmes, B. P. Little, G. Rubin and N. Sverzellati, "COVID-19 Imaging: What We Know Now and What Remains Unknown," Radiology, vol. 299, no. 3, 2021.

[6] Mark I. Neuman, Edward Y. Lee, Sarah Bixby, Stephanie Diperna, Jeffrey Hellinger, Richard Markowitz, Sabah Servaes, Michael C. Monuteaux, and Samir S. Shah. Variability in the interpretation of chest radiographs for the diagnosis of pneumonia in children. Journal of Hospital Medicine, 7(4):294–298, oct 2011

[7] Bai HX, Wang R, Xiong Z, Hsieh B, Chang K, Halsey K, Tran TML, Choi JW, Wang DC, Shi LB, Mei J, Jiang XL, Pan I, Zeng QH, Hu PF, Li YH, Fu FX, Huang RY, Sebro R, Yu QZ, Atalay MK, Liao WH. Artificial Intelligence Augmentation of Radiologist Performance in Distinguishing COVID-19 from Pneumonia of Other Origin at Chest CT. Radiology. 2020 Sep;296(3):E156-E165. doi: 10.1148/radiol.2020201491. Epub 2020 Apr 27. Erratum in: Radiology. 2021 Apr;299(1):E225. PMID: 32339081; PMCID: PMC7233483.

[8] Li L, Qin L, Xu Z, Yin Y, Wang X, Kong B, Bai J, Lu Y, Fang Z, Song Q, Cao K, Liu D, Wang G, Xu Q, Fang X, Zhang S, Xia J, Xia J. Using Artificial Intelligence to Detect COVID-19 and Community-acquired Pneumonia Based on Pulmonary CT: Evaluation of the Diagnostic Accuracy. Radiology. 2020 Aug;296(2):E65-E71. doi: 10.1148/radiol.2020200905. Epub 2020 Mar 19. PMID: 32191588; PMCID: PMC7233473.

[9] Zhang R, Tie X, Qi Z, Bevins NB, Zhang C, Griner D, Song TK, Nadig JD, Schiebler ML, Garrett JW, Li K, Reeder SB, and Chen GH. Diagnosis of COVID-19 Pneumonia Using Chest Radiography: Value of Artificial Intelligence. Radiology 2020.

[10] Oh Y, Park S, Ye JC. Deep Learning COVID-19 Features on CXR Using Limited Training Data Sets. IEEE Trans Med Imaging. 2020 Aug;39(8):2688-2700. doi: 10.1109/TMI.2020.2993291. Epub 2020 May 8. PMID: 32396075.

[11] Wehbe RM, Sheng J, Dutta S, Chai S, Dravid A, Barutcu S, Wu Y, Cantrell DR, Xiao N, Allen BD, MacNealy GA, Savas H, Agrawal R, Parekh N, Katsaggelos AK. DeepCOVID-XR: An Artificial Intelligence Algorithm to Detect COVID-19 on Chest Radiographs Trained and Tested on a Large U.S. Clinical Data Set. Radiology. 2021 Apr;299(1):E167-E176. doi: 10.1148/radiol.2020203511. Epub 2020 Nov 24. PMID: 33231531; PMCID: PMC7993244.

[12] Sun J, Peng L, Li T, Adila D, Zaiman Z, Melton-Meaux GB, Ingraham NE, Murray E, Boley D, Switzer S, Burns JL, Huang K, Allen T, Steenburg SD, Gichoya JW, Kummerfeld E, Tignanelli CJ. Performance of a Chest Radiograph AI Diagnostic Tool for COVID-19: A Prospective Observational Study. Radiol Artif Intell. 2022 Jun 1;4(4):e210217. doi: 10.1148/ryai.210217. PMID: 35923381; PMCID: PMC9344211.

[13] Lessmann N, Sánchez CI, Beenen L, Boulogne LH, Brink M, Calli E, Charbonnier JP, Dofferhoff T, van Everdingen WM, Gerke PK, Geurts B, Gietema HA, Groeneveld M, van Harten L, Hendrix N, Hendrix W, Huisman HJ, Išgum I, Jacobs C, Kluge R, Kok M, Krdzalic J, Lassen-Schmidt B, van Leeuwen K, Meakin J, Overkamp M, van Rees Vellinga T, van Rikxoort EM, Samperna R, Schaefer-Prokop C, Schalekamp S, Scholten ET, Sital C, Stöger JL, Teuwen J, Venkadesh KV, de Vente C, Vermaat M, Xie W, de Wilde B, Prokop M, van Ginneken B. Automated Assessment of COVID-19 Reporting and Data System and Chest CT Severity Scores in Patients Suspected of Having COVID-19 Using Artificial Intelligence. Radiology. 2021 Jan;298(1):E18-E28. doi: 10.1148/radiol.2020202439. Epub 2020 Jul 30. PMID: 32729810; PMCID: PMC7393955.

[14] Dayan, I., Roth, H.R., Zhong, A. et al. Federated learning for predicting clinical outcomes in patients with COVID-19. Nat Med 27, 1735–1743 (2021). https://doi.org/10.1038/s41591-021-01506-3

[15] Zhang R, Tie X, Garrett JW, Griner D, Qi Z, Bevins N, Reeder SB, and Chen GH. A Generalizable Artificial Intelligence Model for COVID-19 Classification Task Using Chest X-ray Radiographs: Evaluated Over Four Clinical Datasets with 15,097 Patients. arXiv preprint arXiv:2210.02189 (2022).

[16] M. d. l. I. Vayá, J. M. Saborit-Torres, J. A. M. Serrano, E. Oliver-Garcia, A. Pertusa, A. Bustos, M. Cazorla, J. Galant, X. Barber, D. Orozco-Beltrán, F. García-García and M. Caparrós, "BIMCV COVID-19+: a large annotated dataset of RX and CT images from COVID-19 patients," IEEE Dataport, 2021.

[17] https://www.rsna.org/education/ai-resources-and-training/ai-image-challenge/covid-19-al-detection-challenge-2021

[18] Simonyan, K. & Zisserman, A. Very deep convolutional networks for large-scale image recognition. arXiv preprint arXiv:1409.1556 (2014).

[19] Iandola, Forrest N; Han, Song; Moskewicz, Matthew W; Ashraf, Khalid; Dally, William J; Keutzer, Kurt. "SqueezeNet: AlexNet-level accuracy with 50x fewer parameters and <0.5MB model size". arXiv:1602.07360 (2016)

[20] Huang, G., Liu, Z., Van Der Maaten, L. & Weinberger, K. Q. Densely connected convolutional networks. in Proceedings of the IEEE conference on computer vision and pattern recognition 4700–4708 (2017).

[21] Tan, M. and Le, Q.V. (2019) EfficientNet: Rethinking Model Scaling for Convolutional Neural Networks. Proceedings of the 36th International Conference on Machine Learning, ICML 2019, Long Beach, 9-15 June 2019, 6105-6114.

The source code is available at https://github.com/xtie97/COVID-19-classification-and-detection

[22] Liu, Z. et al. Swin transformer: Hierarchical vision transformer using shifted windows. in Proceedings of the IEEE/CVF International Conference on Computer Vision 10012–10022 (2021).
[23] Deng J, Dong W, Socher R, Li LJ, Li K, Li FF. ImageNet: A large-scale hierarchical image database. In: 2009 IEEE Conference on Computer Vision and Pattern Recognition, Miami, FL, June 20–25, 2009. Piscataway, NJ: IEEE, 2009.
[24] Wang X, Peng Y, Lu L, Lu Z, Bagheri M, Summers RM. ChestX-ray8: Hospital-scale Chest X-ray Database and Benchmarks on Weakly-Supervised Classification and Localization of Common Thorax Diseases. IEEE CVPR 2017.
[25] D. P. Kingma and J. Ba. Adam: A method for stochastic optimization. arXiv preprint arXiv:1412.6980, 2014
[26] https://github.com/ultralytics/yolov5
[27] Tsung-Yi Lin, Maire, M., Belongie, S. J., Bourdev, L. D., Girshick, R. B., Hays, J., … Zitnick, C. L. (2014). Microsoft COCO: Common Objects in Context. CoRR, abs/1405.0312. Retrieved from http://arxiv.org/abs/1405.0312
[28] https://kaggle.com/competitions/rsna-pneumonia-detection-challenge
[29] Baltruschat I, Steinmeister L, Nickisch H, Saalbach A, Grass M, Adam G, Knopp T, Ittrich H. Smart chest X-ray worklist prioritization using artificial intelligence: a clinical workflow simulation. Eur Radiol. 2021 Jun;31(6):3837-3845. doi: 10.1007/s00330-020-07480-7. Epub 2020 Nov 21. PMID: 33219850; PMCID: PMC8128725.
[30] Gaskin CM, Patrie JT, Hanshew MD, Boatman DM, McWey RP. Impact of a Reading Priority Scoring System on the Prioritization of Examination Interpretations. AJR Am J Roentgenol. 2016 May;206(5):1031-9. doi: 10.2214/AJR.15.14837. Epub 2016 Mar 21. PMID: 26999578.
[31] Shaoqing Ren, Kaiming He, Ross Girshick, and Jian Sun, Faster R-CNN: Towards Real-Time Object Detection with Region Proposal Networks, NIPS'15 Proceedings, arXiv:1506.01497 (2015).
[32] K. He, G. Gkioxari, P. Dollár and R. Girshick, "Mask R-CNN," 2017 IEEE International Conference on Computer Vision (ICCV), 2017, pp. 2980-2988, doi: 10.1109/ICCV.2017.322.

The source code is available at https://github.com/xtie97/COVID-19-classification-and-detection